

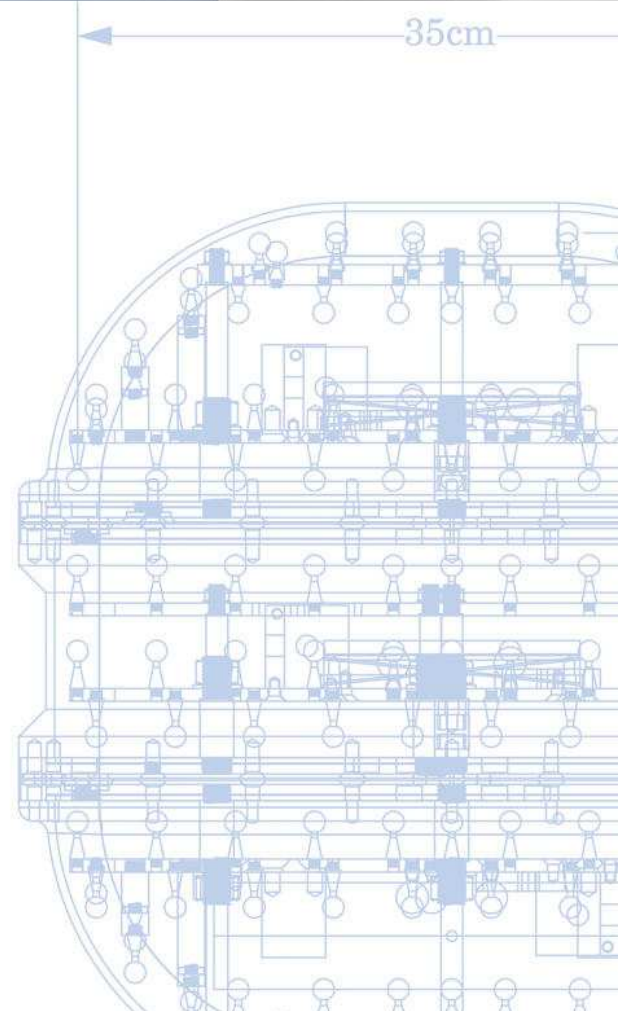
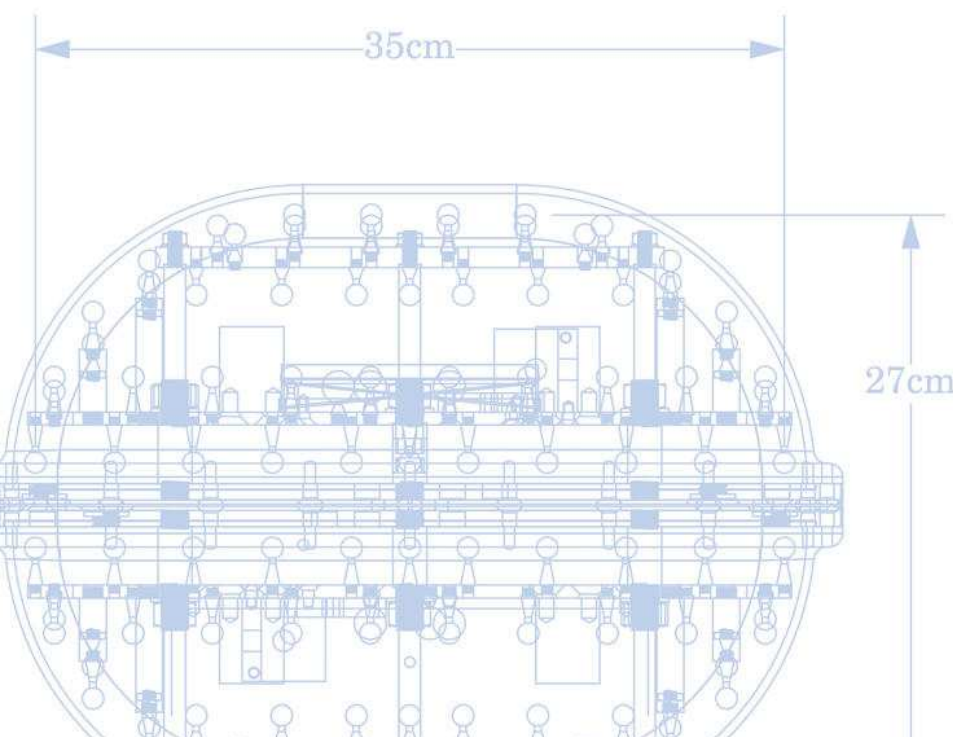
Magphan® RT

MR Imaging QA Designed for Radiotherapy

An integrated phantom and analysis system with a modular, easy-to-handle design

The growing use of MRI for radiation therapy promises many benefits for treatment accuracy and, ultimately, patient outcomes. However, along with these benefits come challenges in accurately characterizing distortion and other critical imaging parameters.

The Phantom Laboratory proudly introduces the Magphan RT system that combines a unique, easy-to-handle phantom design with intuitive and accurate analysis from Image Owl for a tool that will become an indispensable part of your QA suite.



Concurrent multimodality image segmentation by active contours for radiotherapy treatment planning^{a)}

Issam El Naqa,^{b)} Deshan Yang, Aditya Apte, Divya Khullar, Sasa Mutic, Jie Zheng, Jeffrey D. Bradley, Perry Grigsby, and Joseph O. Deasy

Department of Radiation Oncology, School of Medicine, Washington University, St. Louis, Missouri 63110

(Received 18 December 2006; revised 24 September 2007; accepted for publication 24 September 2007; published 20 November 2007)

Multimodality imaging information is regularly used now in radiotherapy treatment planning for cancer patients. The authors are investigating methods to take advantage of all the imaging information available for joint target registration and segmentation, including multimodality images or multiple image sets from the same modality. In particular, the authors have developed variational methods based on multivalued level set deformable models for simultaneous 2D or 3D segmentation of multimodality images consisting of combinations of coregistered PET, CT, or MR data sets. The combined information is integrated to define the overall biophysical structure volume. The authors demonstrate the methods on three patient data sets, including a nonsmall cell lung cancer case with PET/CT, a cervix cancer case with PET/CT, and a prostate patient case with CT and MRI. CT, PET, and MR phantom data were also used for quantitative validation of the proposed multimodality segmentation approach. The corresponding Dice similarity coefficient (DSC) was 0.90 ± 0.02 ($p < 0.0001$) with an estimated target volume error of $1.28 \pm 1.23\%$ volume. Preliminary results indicate that concurrent multimodality segmentation methods can provide a feasible and accurate framework for combining imaging data from different modalities and are potentially useful tools for the delineation of biophysical structure volumes in radiotherapy treatment planning. © 2007 American Association of Physicists in Medicine. [DOI: [10.1118/1.2799886](https://doi.org/10.1118/1.2799886)]

Key words: Multimodality imaging, segmentation, active contours, treatment planning

I. INTRODUCTION

In the era of image-guided adaptive radiotherapy, there has been increased usage of multimodality imaging in radiotherapy treatment planning, diagnosis, and staging of many cancer sites.^{1–3} Historically, kilovoltage x-ray computed tomography (kV-CT) has been considered the standard modality for treatment planning in 3D conformal or intensity-modulated radiation therapy because of its ability to provide photon density information for heterogeneous dose calculations.^{4,5} However, additional information from other modalities, in particular for target volume delineation, has been demonstrated to be useful.^{1,3,6–11} Better soft tissue contrasts can often be acquired from magnetic resonance imaging (MRI), but MRI suffers from spatial distortion and does not provide tissue density information. On the other hand, physiological information (tumor metabolism, proliferation, necrosis, hypoxic regions, etc.) can be collected from nuclear/molecular imaging modalities such as single photon emission computed tomography (SPECT) and positron emission tomography (PET), but both suffer from limited spatial resolution. The complementary nature of these different modalities has led to direct efforts toward combining their information to achieve better radiotherapy treatment planning. For instance, PET/CT has been utilized for staging, planning, and assessment of response to radiation therapy in lung, gynecological, and colorectal cancers.^{1,3,6–11} MRI and MRS combined with CT has been applied in treatment planning of prostate cancers.^{12,13} An institutional clinical trial by Messa

et al. for PET/CT volume delineation in nonsmall cell lung cancer resulted in differences in most patients' clinical target volume definitions based on CT alone.¹⁴ Bradley *et al.* have recently demonstrated that a significant reduction in observer variability could be achieved by combining PET and CT in lung cancer segmentation.¹ A meta-analysis report¹⁵ from Toloza *et al.* comparing CT and PET for staging of mediastinal nodes has shown that the pooled sensitivities were 57% and 84% for CT and PET, respectively, with specificities of 82% versus 89%. Combined PET/CT resulted in a sensitivity range from 78% to 93% and specificity range from 82% to 95%. Hence, it is predictable that the combination of PET with CT will provide an improvement over CT alone for targeting in radiation therapy.⁶ Moreover, a recent study¹⁶ on fractionated stereotactic radiotherapy for patients with meningioma demonstrated improved target definition by combining physiological information from PET, anatomical structures from CT, and soft tissues from MR, resulting in a 73% proportion of original contour definitions being altered.

The basic idea of this work is to combine complementary information from different modalities to automatically define what will be referred to herein as the “biophysical” structure (e.g., target volume or organ at risk) volume (see Fig. 1). By biophysical we mean to emphasize that the target volume may be defined based on physical (e.g., electron density) as well as biological (e.g., increased glucose metabolism) information. It is assumed in this case that the different multimodality images carry complementary information about the structure of interest.

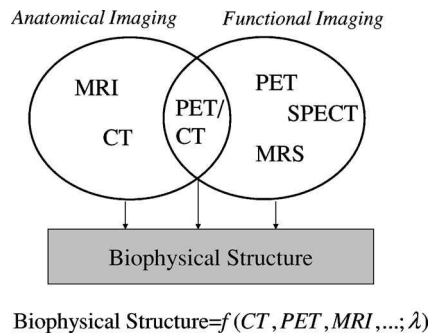


FIG. 1. Multimodality imaging in radiotherapy treatment planning and the definition of the biophysical target as an integration of information from different imaging modalities.

In a routine treatment planning procedure, image segmentation methods are required to distinguish tumors to be treated from surrounding normal tissues that should be spared if possible. Typically, the physician would manually perform the cumbersome target delineation procedure. However, in some cases automated and semiautomated image segmentation techniques are applied. For instance, in a PET clinical review, simple thresholding by using 40% of the standardized-uptake-value (SUV) is applied. However, recent analysis by our group has demonstrated that using simple thresholding to segment PET images in lung cancer would lead to a variation range of 15%–50% in selected threshold value when compared to a CT benchmark.¹⁷ Segmentation is a very challenging problem since it can only be done properly if there is adequate *a priori* knowledge about the data. This *a priori* knowledge could be acquired from the physician's extensive learning experience. A potential alternative approach is to start applying more sophisticated image segmentation methods that can embed this understanding. This problem becomes more demanding with multimodality imaging. Most, if not all, currently proposed autosegmentation methods focus on single modality segmentation, which is by itself a challenging task.^{18–21} A review of segmentation methods in radiotherapy treatment planning could be found in Bondiau *et al.*²² We conjecture that by integrating multimodality images into the same autosegmentation process we will actually improve the robustness of the segmentation process, potentially making it less likely for tumor tissue to be missed or for the noise in any one image to lead to misinterpretation. However, images of different modalities are typically misaligned,²³ which could cause serious problems for the segmentation algorithm, even when manual delineation is used.²⁴ Therefore, our long-term objective is to develop a unified paradigm for handling both registration and segmentation problems for multimodality images. We believe that both problems are intertwined and should be addressed in the same framework, so the segmentation algorithm could benefit from accurate registration results and vice versa (see Fig. 2).^{25,26} In order to make our development efforts more feasibly possible, we shall limit our focus to the demanding problem of multimodality segmentation, where registration,

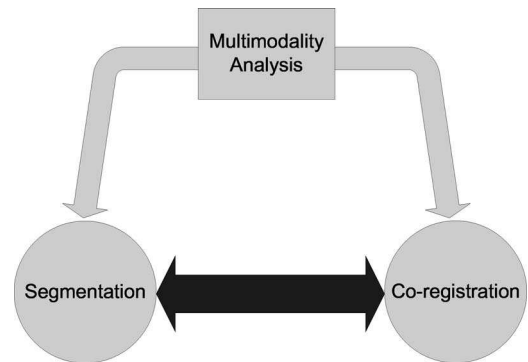


FIG. 2. Multimodality image analysis framework showing the intertwining between image segmentation and image registration.

whether rigid or deformable, is applied as a preprocessing step.

In this work, we developed a multimodality segmentation technique based on generalized single-modality variational methods and active contour deformable models.^{27–30} In addition, prior shape preferences and expert knowledge can be incorporated into these deformable models, as we show in the results section, increasing robustness to image noise and boundary gaps. These methods also have inherent subpixel accuracy due to their spatially continuous representation. Furthermore, the multimodality structure allows the algorithm to work well in the presence of nonuniform uptakes, partial volume effects, and small misregistration errors.

This work is a continuation of our previous efforts on multispectral segmentation, where we have applied various clustering methods to segment multispectral MR images to compute biomechanical properties (stress/strain) to identify physiological functionality of the carotid and coronary heart diseases.³¹ In the clustering approach, intensity vectors were constructed from available MRI images (*T1*-weighted, *T2*-weighted, proton density, etc) at each pixel. Then, the different tissues (lumen, lipid, fibrosis, calcifications) were identified and compared with histology. Clustering was performed using *K*-means and Fuzzy *C*-mean algorithms. However, a significant problem that arose for this approach was the lack of a continuous boundary or a spatial neighborhood concept. To partially alleviate this issue, we applied postprocessing smoothing using morphological operators. Yet, this artificial correction often created undesirable artifacts and would lead to inaccurate segmentation results. Therefore, our recent efforts have focused on applying a new generalization of a geometric deformable model known as the multivalued level set (MVLS) method,^{32,33} which enjoys inherently spatial continuity and topological adaptation such as splitting or merging of target object parts.

In this study, we demonstrate this multimodality segmentation approach for delineating target objects by combining complementary information from different imaging modalities, and thus concurrently identify what we refer to here as the “biophysical structure.” Mathematically, this could be

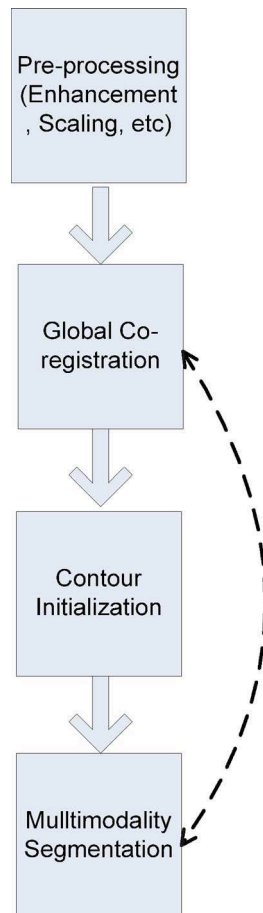


FIG. 3. A block diagram of the proposed concurrent multimodality segmentation method. The method starts by preprocessing of the different images to reduce noise and correct for artifacts. Next, the images are fused using a coregistration method (rigid or deformable). Then, the concurrent segmentation starts by identifying the region-of-interest (a sphere is used unless prior knowledge is emphasized) and iteratively segmenting the biophysical target by integrating information from various imaging modalities until the convergence criteria is satisfied.

thought of as a mapping from the imaging space to the radiologists/oncologists “interpretation” space of the structure boundary

$$\text{Biophysical structure} = f(\text{CT}, \text{PET}, \text{MRI}, \dots; \lambda), \quad (1)$$

where $f(\cdot)$ is a mapping functional that takes the imaging information as input arguments and λ is a set of expert user’s weighting parameters, to identify the underlying biophysical structure of interest based on learned contributions from the different multimodality images. The structure could be either normal tissue or a tumor target volume.

II. MATERIAL AND METHODS

The proposed method was evaluated using clinical data from three different sites, along with physical phantom data. The concurrent multimodality segmentation algorithm consists of four basic steps (Fig. 3): (1) preprocessing for image enhancement, (2) coregistration of the images, (3) contour initialization, and (4) concurrent segmentation of the multimodality images.

II.A. Data sets

II.A.1. Clinical data

The method was evaluated on three patient cases of non-small cell lung cancer using FDG-PET/CT (Fig. 5); cervix cancer using FDG-PET/CT (Figs. 6 and 7); and prostate patient using CT/MR (Fig. 8). In the lung case, the PET image had $5.2 \times 5.2 \times 3.4 \text{ mm}^3$ spatial resolution and the CT image had spatial resolution of $0.98 \times 0.98 \times 5 \text{ mm}^3$. In the cervix cancer case, the spatial resolution for PET was $5.3 \times 5.3 \times 3.4 \text{ mm}^3$ and it was $0.98 \times 0.98 \times 5 \text{ mm}^3$ for the corresponding CT. The images in both cases were acquired using the integrated PET/CT Siemens Biograph at the Siteman Cancer Center. In the prostate cancer case, the CT image had a spatial resolution of $0.71 \times 0.71 \times 3 \text{ mm}^3$ and the MR image had a spatial resolution of $0.78 \times 0.78 \times 10 \text{ mm}^3$. The MR image we used was $T1$ -weighted (short repetition and echo times).

II.A.2. Physical phantom data

A commercial phantom was used with a plastic anthropomorphic head of average human size (Fig. 8); it was initially developed for assessment of stereotactic localization accuracy in stereotactic ring-based brain surgery. Our group previously used the phantom for quality assurance of image registration.³⁴ Targets consisting of plastic spheres and rods were placed throughout the cranium section of the phantom. Tap water was used for CT imaging. However, for MRI and PET imaging, the water inside the phantom was doped with CuNO_3 and ^{18}F -FDG, respectively. The conical indentations on spheres and rods, as well as the points on rods, were visible objects for all three imaging modalities. The cold spot spheres were used as segmentation targets [each is 25.4 mm in diameter (8.58 mL)] and the rods were used as landmarks to assist in alignment. The CT data were digitized at $0.94 \times 0.94 \times 3 \text{ mm}^3$; corresponding PET data had a resolution of $2.57 \times 2.57 \times 2.57 \text{ mm}^3$ and MR had a resolution of $0.98 \times 0.98 \times 2 \text{ mm}^3$.

II.B. Active contour models

Deformable models are geometric representations for curves (in 2D) or surfaces (in 3D) that are defined explicitly or implicitly in the imaging domain. These models move (deform) under the influence of internal force-like equations, which are defined within the curve or surface itself, or external forces, which are computed from the image data.^{29,30} The idea is that contours are characterized by sharp variations in the image intensity. Hence, the objective is to match deformed and reference contours by means of energy minimization.^{27,28,30}

In this work, we utilize active contour techniques based on the level set approach. The level set is a variational method, which defines sets of contour values and positions that evolve over time. Level sets were originally developed in curve evolution theory to overcome the limitations encountered in parametric deformable models (e.g., snakes³⁵), such as initialization requirement, generalization to 3D, and

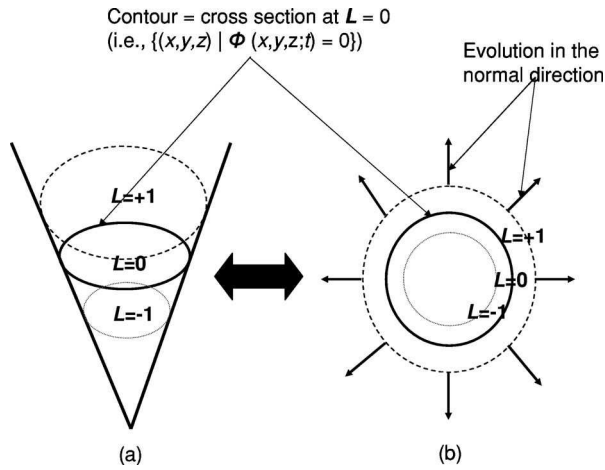


FIG. 4. Deformable image segmentation by the level set method. (a) Representation of the level set surface at time t of the evolving function. (b) A projected view showing the evolution direction. The function ϕ evolves at a velocity proportional to the curvature and inversely proportional to the image gradient. In this example, ϕ is represented with a signed Euclidean distance transform of value L . The contour is extracted at $L=0$ (with negative values inside the contour and positive values outside). This principle is generalized to multimodality images.

topological adaptation, such as splitting or merging of model parts (e.g., delineation of a necrotic tumor). These characteristics have allowed the level set techniques to represent the state-of-the-art in shape recovery applications.^{27,29,36} Mathematically, if the deformable contour/surface at a time $t \geq 0$ is represented by $C(s,t) = \{x(s,t), y(s,t), z(s,t)\}$, $s \in [0, 1]$, then according to the curve evolution theory, its movement could be represented by the following partial differential equation (PDE):²⁹

$$\frac{\partial C(s,t)}{\partial t} = \vec{V}(\kappa), \quad (2)$$

where \vec{V} is the velocity function (of magnitude V) in the normal direction of the contour (\vec{N}) and κ is the local contour curvature, which is defined as divergence along the normal direction of the contour.^{28,29} The level set solution to the problems encountered in snakes (e.g., parameterization and topological adaptation) is achieved by embedding the evolving curve in Eq. (2) in a level set function ϕ . This function defines sets of contour values and positions, including the target boundary at the zero level [$\phi(C)=0$] as shown in Fig. 4. In this case, the evolution equation of Eq. (2) could be rewritten as:

$$\frac{\partial \phi}{\partial t} = V(\kappa)|\nabla \phi| + F(\Theta), \quad (3)$$

where V is defined to be proportional to the curvature and inversely proportional to the image gradient. In this case, the curvature is given by $\text{div}(\nabla \phi / |\nabla \phi|)$.^{28,29} $F(\Theta)$ is a knowledge-based force constraint, where the vector parameter Θ could represent deterministic or statistical shape prior (C^+) information [i.e., assuming Gaussian boundary uncertainty with mean (m) and covariance (Σ)], spring force constraints, and could further potentially incorporate additional

registration parameters.²⁸ The level set function (ϕ) is typically selected as a signed distance function. In our implementation, we used the initial contour drawn by the user as shape prior and the squared-mean intensity difference as spring force as discussed below. Efficient solutions were developed for Eq. (3) by using finite differences and fast marching methods of boundary value problems.²⁹

II.C. Multimodality image segmentation by the level set method

The problem of spatial neighborhood definition encountered in clustering methods is inherently ameliorated in active contour methods. However, the generalization to multimodality imaging is based on redefining the concept of boundary as a logical combination of multiple images. For this reason, we adapted the vectorized or MVLS approach, which was originally developed to handle multichannel color images.^{32,33} In our previous work³⁷ using the level set method for autosegmentation of single images, we noticed that more robust results are achieved when direct gradient-based methods for estimating image boundaries were replaced or combined with methods that do not require using noisy explicit image gradients. Therefore, in our implementation edge-modeling (region-based) techniques (e.g., the Mumford-Shah model) were applied to improve robustness to noise.^{28,38} In this work, we used the following generalization of the level set method^{32,33} for multimodality segmentation of N images:

$$\begin{aligned} \inf_C J(C, c^+, c^-) &\propto \mu \text{ length}(C) \\ &+ \frac{1}{N} \sum_i \lambda_i^+ \int_{\Omega} |I_i - c_i^+|^2 H(\phi) d\mathbf{x} + \lambda_i^- \\ &\times \int_{\Omega} |I_i - c_i^-|^2 (1 - H(\phi)) d\mathbf{x} \\ &+ \frac{1}{N} \sum_i \gamma_i (c_i^+ - c_i^-)^2, \end{aligned} \quad (4)$$

where μ is a weighting factor for the contour length given by the surface integral in 3D (or the line integral in 2D). H is the Heaviside function

$$H(x) = \begin{cases} 1, & x \geq 0 \\ 0, & \text{otherwise} \end{cases}$$

(in the implementation, this is approximated by a smooth inverse tangent function), $c_i^+(c_i^-)$ corresponds to the pixel-intensity means inside (outside) of the contour, and $(\lambda_i^+, \lambda_i^-)$ are user-defined parameter pairs providing relative “importance weights” based on the users’ experience, assigned for each of the imaging modalities in contrast with the other modalities. The last term corresponds to the spring force and is thought to provide further balance by introducing more inside: outside contour contrast by adjusting γ_i .³⁹ \inf_C is the infimum (Infimum is the greatest lower bound of a set. This is more accurate than using the minimum, which does not necessarily exist in this case.) of the set of possible contours

(C) solutions satisfying the functional. Potentially, various logical combinations of images could capture the underlying biophysical structure. In our case, we have chosen to apply what we denote as a soft-AND model. In this soft-AND model, the logical combination of the images is determined by the assigned relative weights (λ_i) in Eq. (4). This could be regarded as a compromise between using a restricted AND model that would only emphasize similar overlapping features between the images and an OR model, which tends to be too flexible allowing probably irrelevant features to be included.^{40,41} The weights are intended to reflect the ability to assign images with lower contrast (i.e., CT) a similar computational importance as images with greater contrast (MRI, PET) based on the user's experience. Nevertheless, other factors may also be important. Obviously, the selection of weights will presumably be based on experience and training gained using the technique and better understanding of the conceptual mapping in Eq. (1).

The MVLS algorithm starts with an initial contour in the multi-image domain; the curve then evolves under the influence of the internal forces (contour curvature and string force) and external forces (image boundaries) until they reach equilibrium. Default weighting (μ) was applied to the contour curvature to maintain acceptable elasticity (smoothness) of the contour and the spring force was fixed for the different imaging modalities. However, notice that the solution to the curve evolution [Eq. (3)] does not necessarily guarantee that the evolving function $\phi(\cdot)$ will remain a valid distance function, which could potentially cause serious numerical problems such as unbounded gradients. Hence, we follow the approach of Aujol *et al.*⁴² in rebuilding the distance function such that the zero level is maintained at the current solution for the evolving function $\phi(C, t_c)$,

$$\frac{\partial \hat{\phi}}{\partial t} + \text{sign}(\phi(C, t_c)(|\nabla \hat{\phi}| - 1)) = 0, \quad (5)$$

where the PDE in Eq. (5) is initialized with the current level set solution at time t_c [i.e., $\hat{\phi}(C, 0) = \phi(C, t_c)$] and the solution $\hat{\phi}$ (as t tends to infinity) would yield the evolving function with corrected distance function that will be used to reinitialize Eq. (3). Upwinding finite difference schemes were used to approximate $|\nabla \hat{\phi}|$, where a one-sided (backward or forward) finite difference is used in accordance with the sign of $\phi(C, t_c)$.²⁷ This reinitialization process is repeated every 10 or 20 iterations.

II.D. Quality validation metrics

We used normalized mutual information (NMI) to evaluate the quality of multimodality registration. This is an information-theoretic approach, which is more robust and effective than intensity-based techniques (e.g., squared difference and correlation) for registration of different modalities images.⁴³ The normalized mutual information for two images (A and B) is given by^{43,44}

$$\text{NMI} = \frac{H(A) + H(B)}{H(A, B)}, \quad (6)$$

where $H(\cdot)$ is the Shannon entropy. The mutual information (MI) is maximized when the images are correctly aligned. In other words, the entropy (or dispersion) is minimized for the joint probability distribution of their intensity values. The rationale for using normalized MI is that it provides more robustness for measuring registration misalignment than simple MI and is less sensitive to changes in the size of overlap region between the two images.⁴⁴

For the validation of segmentation quality, we adopted a spatial overlap index known as the Dice similarity coefficient (DSC). We prefer this metric to reporting volumes only, as commonly practiced, because it takes into account the spatial dependency. DSC is defined in terms of pixel ratio of the overlapping regions^{45,46}

$$\text{DSC} = \frac{2(A \cap B)}{(A + B)}, \quad (7)$$

where at any given threshold DSC values would range from 0, indicating no spatial overlap between two sets of binary segmentation results, to 1 indicating complete overlap. DSC is a special case of the kappa statistics commonly used in reliability analysis to measure observers' agreement.⁴⁷ For purposes of statistical hypothesis testing, a logit [$\text{logit}(x) = \ln(x/1-x)$] transformation is applied to map DSC from the domain of $[0, 1]$ to the unbounded range $(-\infty, \infty)$. The transformed DSC values, under reasonable assumptions, follow an asymptotic normal distribution.⁴⁸ A DSC value greater than 0.7 (i.e., $\text{logit}(\text{DSC}) > 0.847$) has been reported to indicate good segmentation performance.⁴⁵

III. EXPERIMENTAL RESULTS

To evaluate the properties of the proposed multimodality segmentation approach, we demonstrated its performance qualitatively on clinical data and quantitatively on physical phantom data.

III.A. Application to clinical multimodality data

The biophysical structure was identified as the pathological tumor in the PET/CT lung and cervix cases, and the prostate organ in the MRI/CT case. Comparison with available benchmarks was also presented for demonstrative purposes.

In the case of the lung PET/CT shown in Fig. 5, the data were collected using an integrated PET/CT machine; moreover, we applied a rigid body mutual information registration algorithm to correct for possible patient setup shift between images, where the NMI improved slightly from 1.21 to 1.22. The PET images are corrected for motion artifacts using a deconvolution-based technique with a locally derived motion kernel from 4D-CT data.⁴⁹ We selected the larger tumor (subject's right) for multimodality analysis. For comparison purposes, our thoracic oncologist (J.D.B.) provided blinded definition of the gross tumor volume on CT, PET, and the fused PET/CT separately for each case using the manual

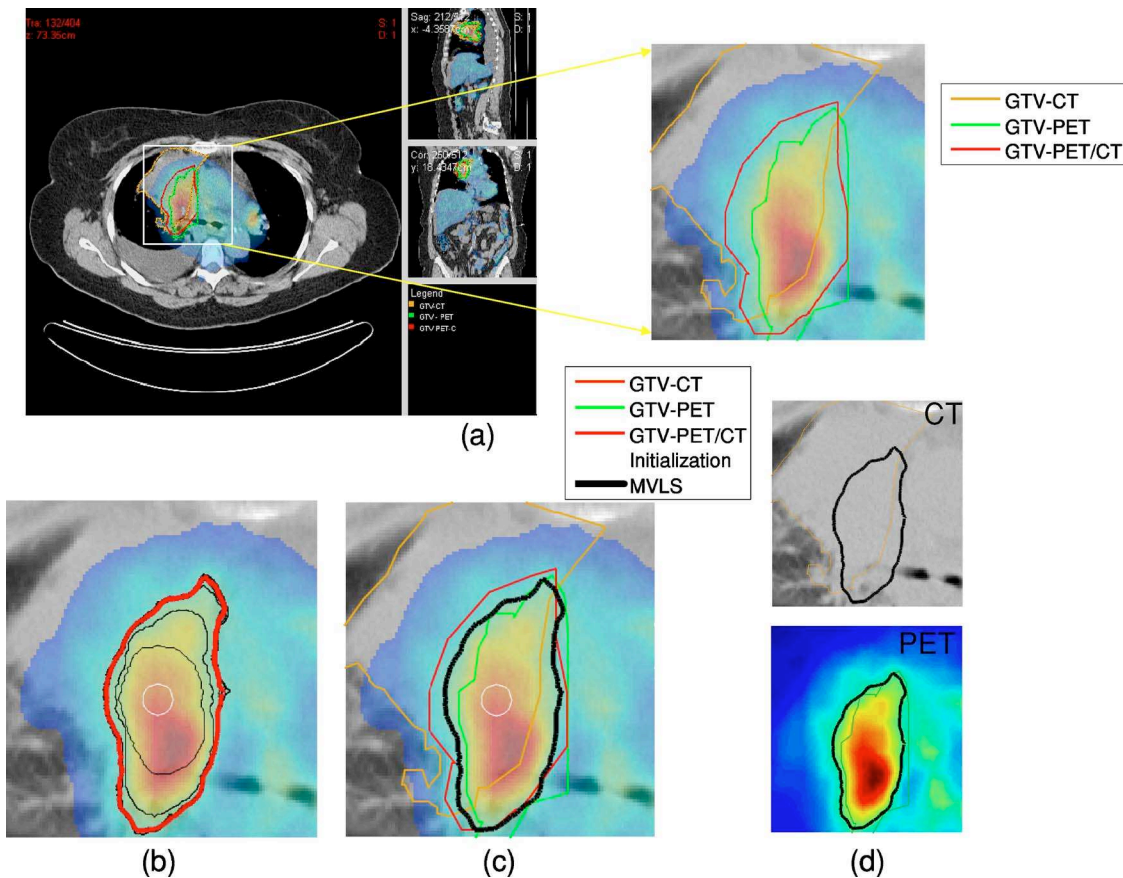


FIG. 5. Analysis of lung PET/CT case. (a) A fused PET/CT displayed in CERR with manual contouring shown of the subject's right gross tumor volume. The contouring was performed separately for CT (in orange), PET (in green), and fused PET/CT (in red) images. (b) The MVLS algorithm was initialized with a circle (in white) of 9.8 mm diameter, evolved contour is steps of ten iterations (in black), and the final estimated contour (in thick red). The algorithm converged in 120 iterations in a few seconds. The PET/CT ratio weighting was selected as 1:1.65. (c) MVLS results is shown along with manual contour results on the fused PET/CT. Note the agreement of fused PET/CT manual contour and MVLS (DSC=0.87). (d) MVLS contour superimposed on CT (top) and PET (bottom) separately.

contouring tools available with Computational Environment for Radiotherapy Research (CERR) as shown in Fig. 5(a).⁵⁰ In Fig. 5(b), we initialized the MVLS algorithm with a generic circle (in white) of 9.8 mm diameter. The evolved contour in steps of ten iterations (in black) and the final estimated contour (in thick red) are shown. The MVLS algorithm converged in 120 iterations in a few seconds. In Fig. 5(c), we superimposed the MVLS results with the manual contouring results on the fused PET/CT. The MVLS achieved DSC values of 0.44 with manual CT contouring [Fig. 5(d), top], 0.84 with PET [Fig. 5(d), bottom], and 0.87 with fused PET/CT. Note that the MVLS tended to mimic the physician response by moving the contour more to the left incorporating this information from the CT.

Similarly, in the case of cervix PET/CT (Fig. 6), the coregistered PET/CT was corrected for possible patient setup errors with a slight NMI improvement from 1.22 to 1.23. The PET image was sharpened using deconvolution.³⁷ The 40% maximum SUV thresholding is adopted in our institute to estimate gross tumor volume for cervix cancer patients due to the high target to background ratio of these tumors in PET and the difficulty to distinguish their boundary in CT.⁵¹ This is different from the lung case, where such criteria suffers

from significant variability as discussed earlier.¹⁷ In Fig. 6(b), the MVLS algorithm is initialized with a circle (in white) of 15.9 mm diameter. The evolved contour took ten iterations (in blue) and the final estimated contours (in thick black) are shown. The MVLS algorithm converged in just 30 iterations. This fast convergence could be attributed in part to the almost spherical shape of the tumor and the sharpness of the gradient. It is noticed that the results of the MVLS matches the PET ground truth (99%) as shown in Fig. 6(c). Hence, the delineation results were explained mainly by PET in this case as shown in Fig. 6(d), although information from CT could still be used to steer the algorithm, if desired. The MVLS algorithm is directly generalizable to a 3D surface structure as shown in Fig. 7. In this case, the algorithm converged in 1.2 s.

A more challenging case was the analysis of prostate MRI/CT shown in Fig. 8(a). In Fig. 8(b), we show a checkerboard of the coregistration process of T1-MRI with CT using rigid body mutual information algorithm. The NMI improved from 1.07 to 1.11. The results of this example seem to be more dependent on the initial shape; hence, the initial contour (in white) was emphasized in the algorithm as

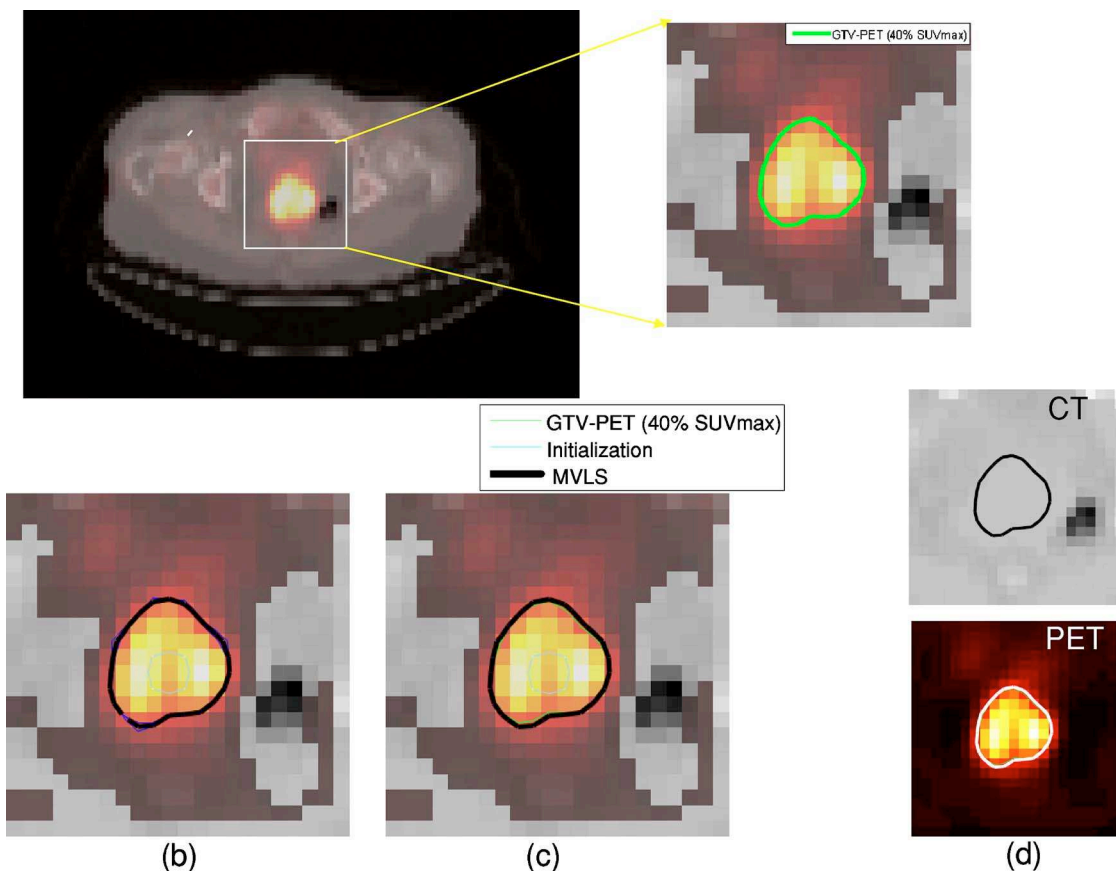


FIG. 6. Analysis of cervix PET/CT. (a) Coregistered PET/CT after correction for small hardware misalignment with mutual information increasing from 1.22 to 1.23. The 40% maximum SUV contour (in green) is shown in the region-of-interest. (b) The MVLS algorithm is initialized with a circle (in white) of 15.9 mm diameter, curve evolution in steps of ten iterations (in blue), and the final estimated contour (in thick black). The algorithm converged in 30 iterations. This quick convergence is by part due to the deformed circular shape of the tumor and the PET sharp gradient. The PET/CT ratio weighting was selected as 1:1.25. (c) MVLS result is shown along with 40% SUV contour on the fused PET/CT. Note the high agreement as expected. (d) MVLS contour superimposed on CT (top) and PET (bottom). The PET/CT ratio weighting was selected as 1:1.25.

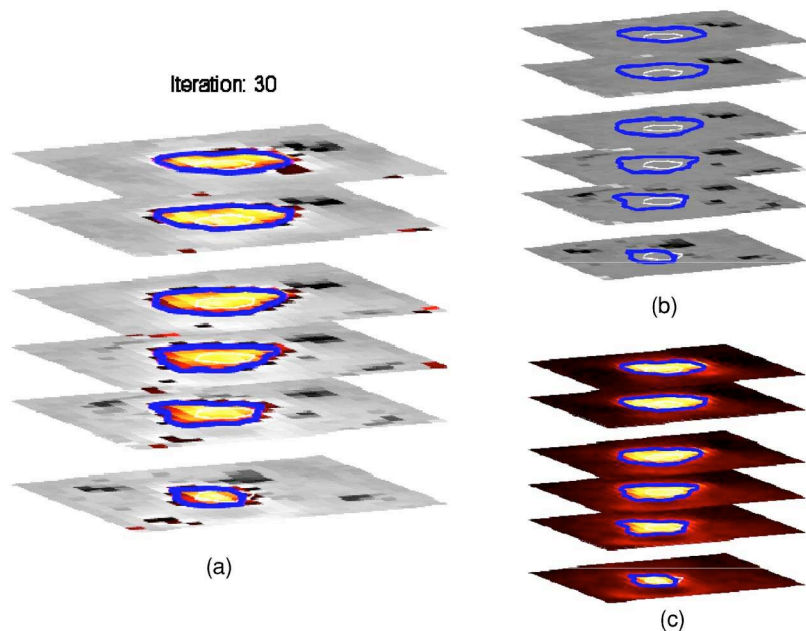


FIG. 7. A 3D generalization of the MVLS algorithm in the case of PET/CT cervix. Different slices of the 3D volume of the PET/CT data are shown. (a) The data were fused for display (foreground PET and background CT). The MVLS algorithm is initialized with a sphere (in light blue) of 15.9 mm diameter, curve evolution in steps of ten iterations (in magenta), and the final estimated contour (in thick dark blue). The algorithm converged in 30 iterations. (b) MVLS estimated contour superimposed on CT. (c) MVLS estimated contour superimposed on PET.

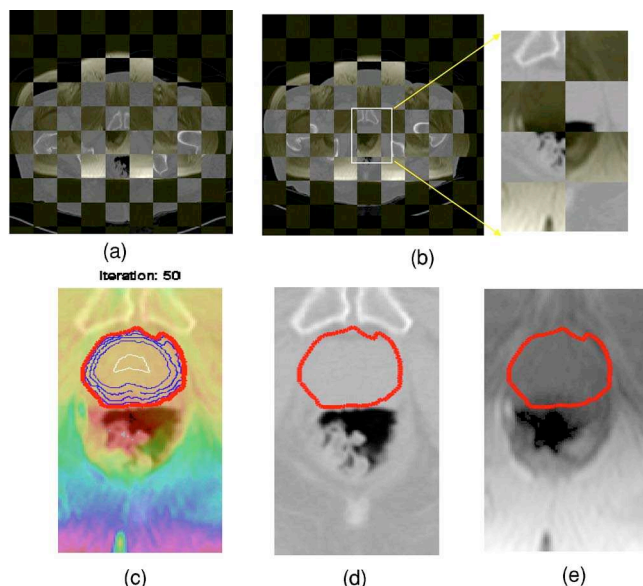


FIG. 8. Analysis of prostate MRI/CT. (a) Checkerboard display of the original MRI/CT. (b) Coregistered MRI/CT using a NMI algorithm, which increased NMI from 1.07 to 1.11. Right: selected region-of-interest containing the prostate which is chosen as the target for multimodality analysis. (c) Overlaid display of MRI/CT (foreground is MR and background in gray scale is the CT). In the figure, we show initially drawn contour (in white). Note in this case using an arbitrary shape might lead to erroneous results. This initial contour is emphasized in the MVLS algorithm as prior knowledge of the prostate shape. Evolved contour is shown (in blue) after ten iterations and the final estimated contour (in thick red). The algorithm converged in 50 iterations. A 1.5:1 MR to CT importance weighting was used in this example. In (d) and (e) we show the MVLS result superimposed on CT (d) and MR (e) for comparison. Note that using other multispectral MR images besides the T1 could potentially provide further useful information to the algorithm.

prior knowledge as shown in Fig. 8(c). We show the MVLS evolved contour in steps of ten iterations (in blue) and the final estimated contour (in thick red). The algorithm converged in 50 iterations (in less than 1 s). The resulting prostate delineation is shown superimposed on CT [Fig. 8(d)] and MR [Fig. 8(e)]. Note that the delineation of prostate on the CT image is significantly improved by incorporating the MR. On the other hand; CT also improved the convergence results on MR by offering additional external force to guide the curve evolution to desired target's boundary.

In all of the previous experiments, images were normalized linearly to a common scale [0–255] before applying the MVLS. This normalization is not intended to change the characteristics of any of the images; however, it provides a common scale for assigning importance weights to the different modalities. PET images were sharpened using deconvolution. In the PET/CT cases we slightly increased the weights λ_i in Eq. (4) (1:1.65 and 1:1.25 ratios for lung and cervix, respectively) corresponding to CT to increase its contribution in the presence of a strong PET signal. In the MR/CT case, we assigned a higher weight (1.5:1 ratio) to MR. Note that these weights are assigned experimentally to match an experienced user's interpretation of the correct contour. Consensus definitions for the true biophysical structures (tumor targets or organs at risk) could be generated by an

expert panel of physicians, as discussed later. Afterwards, these gold standards for delineated volumes would be used to train the algorithm and determine modality weights. If successful, the algorithm could be applied in practice to new cases with minimal user interaction.

III.B. Validation using physical phantom data

The phantom data was first registered manually in CERR,⁵² followed by a rigid body mutual information algorithm using the CT data as reference to simulate treatment planning process (see Fig. 9). This postprocessing step improved NMI between CT and MR from 1.19 to 1.22 and between CT and PET from 1.26 to 1.28. The quantitative evaluation results are summarized in Table I. Table I summarizes the application of the MVLS to the individual modalities and the combined modalities. The DSC similarity metric indicates that MVLS provided good results overall [DSC from 0.74 (CT alone) to 0.9 (CT/MRI/PET)]. The combined CT/PET/MR yielded the superior average segmentation results. It is noted that most of the detection accuracy is provided by the MR data, which provided the highest contrast in this example, while the CT yielded the least accuracy. In terms of volume, the combined PET/CT/MR resulted in the most reliable estimate ($-1.28 \pm 1.231\%$ error in estimated volume). PET had the lowest average error in volume but suffered from large variations. Sample results are shown in Fig. 10.

IV. DISCUSSION

The objective of this study was to explore methods for integrating multiple information streams from different imaging modalities, which automatically define the biophysical structure (tumor target or organ at risk). The use of multimodality imaging for treatment planning is rapidly increasing. In this work, we demonstrated a new approach to automatically integrate multiple image data sets, with complementary information, that is based on utilizing the generalizable properties of the variational level set method. The active contour model of the level set offers several attractive characteristics such as topological adaptation (splitting and merging of model parts such as in the presence of necrotic tumor), computational efficiency (few seconds on a 3 GHz xeon CPU), incorporation of prior knowledge, and spatial continuity in comparison with clustering techniques for multimodality analysis. However, there have been attempts to combine level sets with clustering or classification methods, which act as regularizers to further improve their performance.^{36,53} The multimodality nature of this method allows the algorithm to perform well in the presence of nonuniform uptakes, partial volume effects, or small misregistration errors. It stands to reason that simultaneous use of multimodality images allows for a less uncertain result by the addition of relevant information. Our current analysis of the proposed method suggests acceptable accuracy; a DSC of 0.9 and volume error of less than 2% were estimated when applying the MVLS algorithm to the physical phantom data. In the clinical case examples, the segmentation results agreed well with an experi-

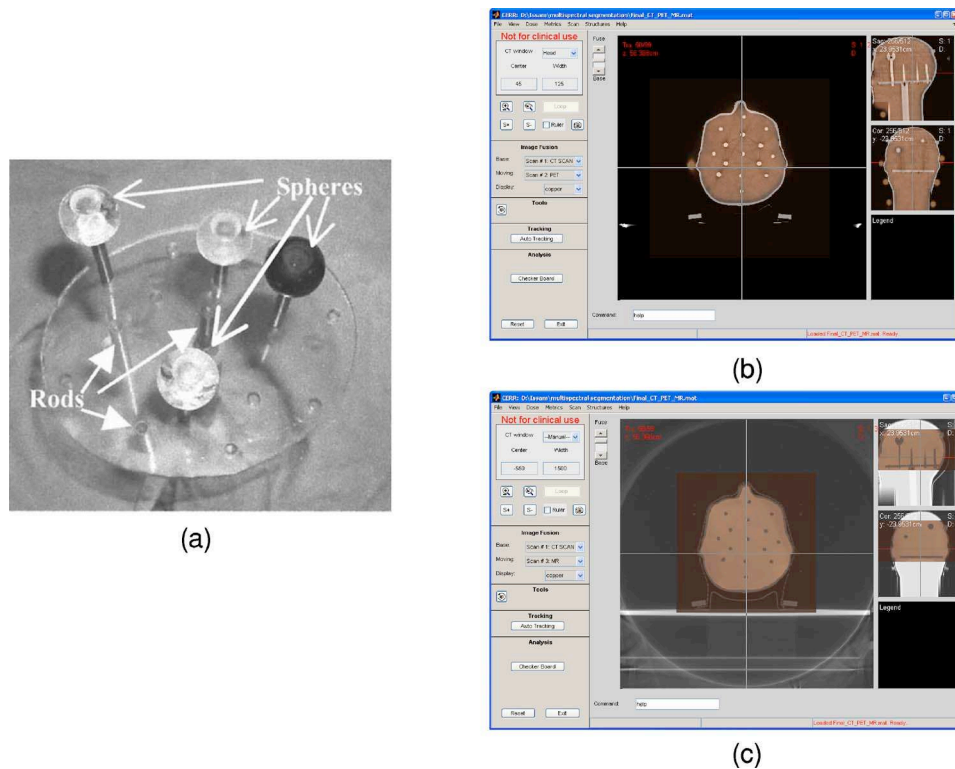


FIG. 9. Physical phantom study. (a) A picture of the anthropomorphic head phantom showing the internal target spheres used to evaluate the MVLS concurrent segmentation algorithm. (b) Registered PET/CT in CERR. (c) Registered MRI/CT in CERR.

enced user's perception of the expected boundaries. In the lung PET/CT, we demonstrated that the fused PET/CT image (not the CT alone + the PET alone) yielded the best agreement with manual contouring. However, most of the information was weighted toward the PET signal. A similar issue was noted for the PET/CT cervix case. Moreover, some studies suggest that using MR for tissue differentiation would be useful in this case.^{54,55} An unanswered subject in image segmentation is the quantification of segmentation accuracy using clinical data, due to the lack of a gold standard. Tissue localization through contouring by experts has often been labeled as the "truth" for the testing of automated algorithms. However, this approach has been reported to suffer from intra- and interobserver variability.^{56,57} Nevertheless, several studies have demonstrated that computer aided detection methods can improve radiologists' performance, essentially by acting as a second reader.⁵⁸

In order to combine complementary information from the different modalities, we have adopted a soft-AND model. This approach provides the user with the flexibility to emphasize semantic knowledge from different modalities based

on prior experience and better understanding of the conceptual definition of the biophysical structure. Ultimately, artificial intelligence and expert system approaches could be used to mimic human interpretation of the biophysical structure and automatically extract the importance weights in the soft-AND model.⁵⁹

Currently, we attempt to register the images before segmentation using rigid affine transforms based on mutual information.⁶⁰ Alternatively, deformable models based on biomechanical principles⁶¹ or extensions of variational methods⁶² could be applied to the registration phase, with likely better results. A further improvement would be to use a joint segmentation and registration approach, where the algorithm alternates between the two processes.^{25,26} However, that approach often has convergence problems due to increased computational complexity and PDE numerical instability that would need to be carefully addressed.

Note that in the lung cancer case, the current proposal could potentially be extended to 4D segmentation by noting that 4D images are typically acquired over consecutive segments of the respiratory cycle from the same scanner (e.g.,

TABLE I. Phantom study evaluation summary of the different metrics (mean, standard deviation) for the four balls boundary detection using MVLS.

	DSC	Logit (DSC) ^a	Estimated volume (mL)	% estimated volume error
CT only	0.74±0.046	1.06±0.240	8.20±0.134	-4.42±1.563
PET only	0.85±0.053	1.74±0.387	8.50±0.500	-0.97±5.828
MR only	0.89±0.018	2.14±0.211	8.19±0.292	-4.59±3.408
CT/PET/MR	0.90±0.017	2.22±0.189	8.47±0.106	-1.28±1.231

^aAll *p* values were significant (*p* < 0.05).

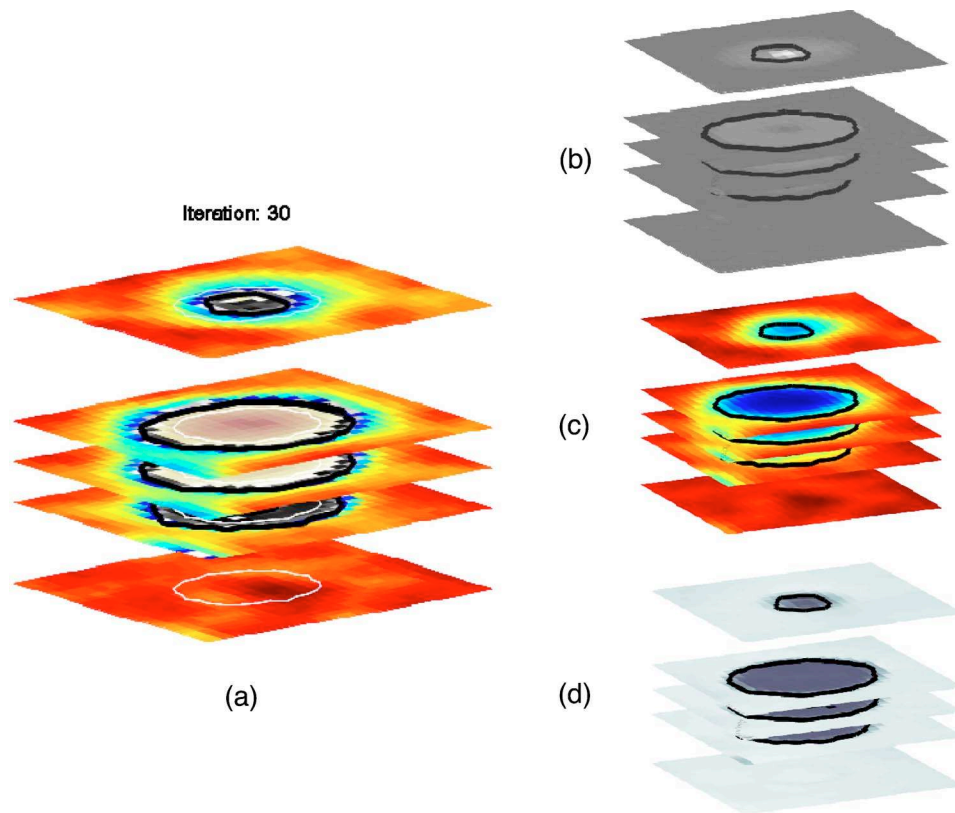


FIG. 10. Sample physical phantom results using the MVLS. Different slices of the 3D volume are shown. (a) The MVLS algorithm is initialized with a sphere (in white) in the fused PET/CTMR domain, curve evolution is shown in steps of ten iterations (in blue), and the final estimated contour (in thick black). The algorithm converged in 30 iterations. Note the accurate capturing of the sphere boundary (black circle) despite the fact that parts of the initial contour lie outside the sphere while others lie inside the sphere. In addition, the algorithm can adapt to topological changes (capturing the hole in the middle of the sphere—or necrotic regions in case of tumors for example—if desired). Only the exterior boundary, however, was used for evaluation purposes. For illustration, the estimated contour is superimposed separately on (b) CT, (c) PET, and (d) MR.

4D CT or 4D PET/CT) and are subsequently sorted into different breathing phases.⁶³ In this case, the MVLS segmentation results of a biophysical structure at a certain breathing phase could be fed as an initialization contour for the following phase. Thus, the segmentation of a biophysical structure of interest is propagated from one phase to another along the breathing cycle in the multimodality domain. In such a case, the algorithm could further benefit from sinogram-based sorting methods, which offers improved registration quality.⁶³

V. CONCLUSIONS

In this work, we have illustrated a new approach to integrate complementary information from multimodality images to better identify the biophysical structure. The method relies on using a generalization of the level set approach. The logical combination of the different multimodalities could be tuned by changing the weights in the model according to user's prior knowledge. Increasing the number of images would potentially improve the capturing of the contour boundary of the targeted biophysical structure. Our simulations indicate that the proposed algorithm is promising and should be further investigated as potential basis of a reliable contouring tool approach for multimodality image-guided treatment planning in radiotherapy.

ACKNOWLEDGMENTS

This research was partially supported by a grant from the American Cancer Society IRG-58-010-50. We would also

like to thank the editor and two anonymous reviewers for thorough evaluation of our work and valuable suggestions.

^{a)}An initial version of this work was presented in the Laughlin Science Council Research Symposium at AAPM, Orlando, FL, 2006.

^{b)}Electronic mail: elnaqa@wustl.edu

¹J. D. Bradley, C. A. Perez, F. Dehdashti, and B. A. Siegel, "Implementing biologic target volumes in radiation treatment planning for non-small cell lung cancer," *J. Nucl. Med.* **45**, 96S–101S (2004).

²C. Rasch, R. Steenbakkers, and M. v. Herk, "Target definition in prostate, head, and neck," *Semin. Radiat. Oncol.* **15**, 136–145 (2005).

³B. Zangheri, C. Messa, M. Picchio, L. Gianolli, C. Landoni, and F. Fazio, "PET/CT and breast cancer," *Eur. J. Nucl. Med. Mol. Imaging* **31**, S135–S142 (2004).

⁴F. M. Khan, *Treatment Planning in Radiation Oncology*, 2nd ed. (Lippincott Williams and Wilkins, Philadelphia, 2007).

⁵S. Webb, *The Physics of Three-Dimensional Radiation Therapy: Conformal Radiotherapy, Radiosurgery, and Treatment Planning* Bristol, UK (Institute of Physics, Philadelphia, 2001).

⁶J. Bradley, W. L. Thorstad, S. Mutic, T. R. Miller, F. Dehdashti, B. A. Siegel, W. Bosch, and R. J. Bertrand, "Impact of FDG-PET on radiation therapy volume delineation in non-small-cell lung cancer," *Int. J. Radiat. Oncol. Biol. Phys.* **59**, 78–86 (2004).

⁷D. L. Schwartz *et al.*, "FDG-PET/CT imaging for preradiotherapy staging of head-and-neck squamous cell carcinoma," *Int. J. Radiat. Oncol. Biol. Phys.* **61**, 129–136 (2005).

⁸I. F. Ciernik, "Radiotherapy of rectal cancer," *Schweiz. Rundsch. Med. Prax.* **93**, 1441–1446 (2004).

⁹P. Lind, I. Igerc, T. Beyer, P. Reinprecht, and K. Hausegger, "Advantages and limitations of FDG PET in the follow-up of breast cancer," *Eur. J. Nucl. Med. Mol. Imaging* **31**, S125–S134 (2004).

¹⁰T. Beyer, D. W. Townsend, T. Brun, P. E. Kinahan, M. Charron, R. Roddy, J. Jerin, J. Young, L. Byars, and R. Nutt, "A combined PET/CT scanner for clinical oncology," *J. Nucl. Med.* **41**, 1369–1379 (2000).

¹¹L. Boucher, S. Rodrigue, R. Lecomte, and F. Benard, "Respiratory gating for 3-dimensional PET of the thorax: Feasibility and initial results," *J. Nucl. Med.* **45**, 214–219 (2004).

- ¹²L. Chen, R. A. Price, Jr., T. B. Nguyen, L. Wang, J. S. Li, L. Qin, M. Ding, E. Palacio, C. M. Ma, and A. Pollack, "Dosimetric evaluation of MRI-based treatment planning for prostate cancer," *Phys. Med. Biol.* **49**, 5157–5170 (2004).
- ¹³G. S. Payne and M. O. Leach, "Applications of magnetic resonance spectroscopy in radiotherapy treatment planning," *Br. J. Radiol.* **79**, S16–S26 (2006).
- ¹⁴C. Messa, G. L. Ceresoli, G. Rizzo, D. Artioli, M. Cattaneo, P. Castellone, V. Gregorc, M. Picchio, C. Landoni, and F. Fazio, "Feasibility of [18F]FDG-PET and coregistered CT on clinical target volume definition of advanced non-small cell lung cancer," *Q. J. Nucl. Med. Mol. Imaging* **49**, 259–266 (2005).
- ¹⁵E. M. Toloza, L. Harpole, and D. C. McCrory, "Noninvasive staging of non-small cell lung cancer: A review of the current evidence," *Chest* **123**, 137S–146S (2003).
- ¹⁶S. Milker-Zabel, A. Zabel-du Bois, M. Henze, P. Huber, D. Schulz-Ertner, A. Hoess, U. Haberkorn, and J. Debus, "Improved target volume definition for fractionated stereotactic radiotherapy in patients with intracranial meningiomas by correlation of CT, MRI, and [68Ga]-DOTATOC-PET," *Int. J. Radiat. Oncol. Biol. Phys.* **65**, 222–227 (2006).
- ¹⁷K. J. Biehl, F. M. Kong, F. Dehdashti, J. Y. Jin, S. Mutic, I. El Naqa, B. A. Siegel, and J. D. Bradley, "18F-FDG PET definition of gross tumor volume for radiotherapy of non-small cell lung cancer: Is a single standardized uptake value threshold approach appropriate?" *J. Nucl. Med.* **47**, 1808–1812 (2006).
- ¹⁸Y. E. Erdi, O. Mawlawi, S. M. Larson, M. Imbriaco, H. Yeung, R. Finn, and J. L. Humm, "Segmentation of lung lesion volume by adaptive positron emission tomography image thresholding," *Cancer* **80**, 2505–2509 (1997).
- ¹⁹V. Pekar, T. R. McNutt, and M. R. Kaus, "Automated model-based organ delineation for radiotherapy planning in prostatic region," *Int. J. Radiat. Oncol. Biol. Phys.* **60**, 973–980 (2004).
- ²⁰N. D. Nanayakkara, J. Samarabandu, and A. Fenster, "Prostate segmentation by feature enhancement using domain knowledge and adaptive region based operations," *Phys. Med. Biol.* **51**, 1831–1848 (2006).
- ²¹S. M. Pizer, P. T. Fletcher, S. Joshi, A. G. Gash, J. Stough, A. Thall, G. Tracton, and E. L. Chaney, "A method and software for segmentation of anatomic object ensembles by deformable m-reps," *Med. Phys.* **32**, 1335–1345 (2005).
- ²²P. Y. Bondiau, G. Malandain, S. Chanalet, P. Y. Marcy, C. Foa, and N. Ayache, "Image processing and radiotherapy," *Cancer Radiother.* **8**, 120–129 (2004).
- ²³J. V. Hajnal, D. J. Hawkes, and D. L. G. Hill, *Medical Image Registration* (CRC Press, Boca Raton, 2001).
- ²⁴J. L. Fox, R. Rengan, W. O'Meara, E. Yorke, Y. Erdi, S. Nehmeh, S. A. Leibel, and K. E. Rosenzweig, "Does registration of PET and planning CT images decrease interobserver and intraobserver variation in delineating tumor volumes for non-small-cell lung cancer?" *Int. J. Radiat. Oncol. Biol. Phys.* **62**, 70–75 (2005).
- ²⁵A. Yezzi, L. Zollei, and T. Kapur, "A variational framework for integrating segmentation and registration through active contours," *Med. Image Anal.* **7**, 171–185 (2003).
- ²⁶K. M. Pohl, J. Fisher, W. E. Grimson, R. Kikinis, and W. M. Wells, "A Bayesian model for joint segmentation and registration," *Neuroimage* **31**, 228–239 (2006).
- ²⁷G. Aubert, *Mathematical Problems in Image Processing: Partial Differential Equations and the Calculus of Variations*, 2nd ed. (Springer, New York, 2006).
- ²⁸S. Osher and R. P. Fedkiw, *Level Set Methods and Dynamic Implicit Surfaces* (Springer, New York, 2003).
- ²⁹J. A. Sethian, *Level Set Methods and Fast Marching Methods: Evolving Interfaces in Computational Geometry, Fluid Mechanics, Computer Vision, and Material Science*, 2nd ed. (Cambridge University Press, Cambridge, 1999).
- ³⁰C. Xu, D. L. Pham, and J. L. Prince, in *Handbook of Medical Imaging: Medical Image Processing and Analysis*, edited by M. Sonka and J. M. Fitzpatrick (SPIE, Bellingham, WA, 2002), Vol. 2, pp. 129–174.
- ³¹J. Zheng, I. El Naqa, F. E. Rowold, T. K. Pilgram, P. K. Woodard, J. E. Saffitz, and D. Tang, "Quantitative assessment of coronary artery plaque vulnerability by high-resolution magnetic resonance imaging and computational biomechanics: A pilot study *ex vivo*," *Magn. Reson. Med.* **54**, 1360–1368 (2005).
- ³²J. Shah, "Curve evolution and segmentation functionals: Application to color images," presented at the International Image Processing Conference, Lausanne, Switzerland, IEEE Int'l Conf. Image Proc., 9, pp. 461–464, 1996.
- ³³T. F. Chan, B. Y. Sandberg, and L. A. Vese, "Active contours without edges for vector-valued images," *J. Vis. Commun. Image Represent.* **11**, 130–141 (2000).
- ³⁴S. Mutic, J. F. Dempsey, W. R. Bosch, D. A. Low, R. E. Drzymala, K. S. Chao, S. M. Goddu, P. D. Cutler, and J. A. Purdy, "Multimodality image registration quality assurance for conformal three-dimensional treatment planning," *Int. J. Radiat. Oncol. Biol. Phys.* **51**, 255–260 (2001).
- ³⁵M. Kass, A. Witkin, and D. Terzopoulos, "Snakes: Active contour models," *Int. J. Comput. Vis.* **1**, 321–331 (1987).
- ³⁶J. S. Suri, L. Kecheng, S. Singh, S. N. Laxminarayan, Z. Xiaolan, and L. Reden, "Shape recovery algorithms using level sets in 2-D/3-D medical imagery: A state-of-the-art review," *IEEE Trans. Inf. Technol. Biomed.* **6**, 8–28 (2002).
- ³⁷I. El Naqa, J. Bradley, J. Deasy, K. Biehl, R. Laforest, and D. Low, "Improved analysis of PET images for radiation therapy," 14th International Conference on the Use of Computers in Radiation Therapy, Seoul, Korea, 2004, ICCR Proceedings 2004, Vol. 1, pp. 361–363.
- ³⁸T. F. Chan and L. A. Vese, "Active contours without edges," *IEEE Trans. Image Process.* **10**, 266–277 (2001).
- ³⁹S. Kulkarni, V. Kumar, and B. N. Chatterji, "Edgeless active contouring, for vector-valued natural image segmentation," presented at the TENCON 2003, 15–17 Oct. Conference on Convergent Technologies for Asia-Pacific Region, IEEE TENCON 2003 Proceedings, Vol. 1, pp. 16–20, 2003.
- ⁴⁰T. Chan, M. Moelich, and B. Sandberg, "Some recent developments in variational image segmentation," Report No. 06–52, UCLA, 2006 (unpublished).
- ⁴¹Y. Young and D. Levy, "Registration-based morphing of active contours for segmentation of CT scans," *Math. Biosci. Eng.* **2**, 79–96 (2005).
- ⁴²J. Aujol and G. Aubert, "Signed distance functions and viscosity solutions of discontinuous Hamilton–Jacobi equations," Technical Report No. 4507, 2002 (unpublished).
- ⁴³J. P. Pluim, J. B. Maintz, and M. A. Viergever, "Mutual-information-based registration of medical images: A survey," *IEEE Trans. Med. Imaging* **22**, 986–1004 (2003).
- ⁴⁴C. Studholme, D. L. G. Hill, and D. J. Hawkes, "An overlap invariant entropy measure of 3D medical image alignment," *Pattern Recogn.* **32**, 71–86 (1999).
- ⁴⁵K. H. Zou, S. K. Warfield, A. Bharatha, C. M. Tempany, M. R. Kaus, S. J. Haker, W. M. Wells III, F. A. Jolesz, and R. Kikinis, "Statistical validation of image segmentation quality based on a spatial overlap index," *Acad. Radiol.* **11**, 178–189 (2004).
- ⁴⁶K. H. Zou, W. M. Wells III, R. Kikinis, and S. K. Warfield, "Three validation metrics for automated probabilistic image segmentation of brain tumours," *Stat. Med.* **23**, 1259–1282 (2004).
- ⁴⁷R. F. Woolson and W. R. Clarke, *Statistical Methods for the Analysis of Biomedical Data*, 2nd ed. (Wiley-Interscience, New York, 2002).
- ⁴⁸A. Agresti, *Categorical Data Analysis*, 2nd ed. (Wiley-Interscience, New York, 2002).
- ⁴⁹I. El Naqa, D. Low, J. Bradley, M. Vivic, and J. Deasy, "Deblurring of breathing motion artifacts in thoracic PET images by deconvolution methods," *Med. Phys.* **33**, 3587–3600 (2006).
- ⁵⁰J. O. Deasy, "Denoising of electron beam Monte Carlo dose distributions using digital filtering techniques," *Phys. Med. Biol.* **45**, 1765–1779 (2000).
- ⁵¹T. R. Miller and P. W. Grigsby, "Measurement of tumor volume by PET to evaluate prognosis in patients with advanced cervical cancer treated by radiation therapy," *Int. J. Radiat. Oncol. Biol. Phys.* **53**, 353–359 (2002).
- ⁵²J. O. Deasy, A. I. Blanco, and V. H. Clark, "CERR: A computational environment for radiotherapy research," *Med. Phys.* **30**, 979–985 (2003).
- ⁵³F. Zhuge, G. D. Rubin, S. Sun, and S. Napel, "An abdominal aortic aneurysm segmentation method: Level set with region and statistical information," *Med. Phys.* **33**, 1440–1453 (2006).
- ⁵⁴N. M. deSouza, R. Dina, G. A. McIndoe, and W. P. Soutter, "Cervical cancer: Value of an endovaginal coil magnetic resonance imaging technique in detecting small volume disease and assessing parametrial extension," *Gynecol. Oncol.* **102**, 80–85 (2006).
- ⁵⁵K. Narayan, A. McKenzie, R. Fisher, B. Susil, T. Jobling, and D. Bernshaw, "Estimation of tumor volume in cervical cancer by magnetic resonance imaging," *Am. J. Clin. Oncol.* **26**, e163–e168 (2003).

- ⁵⁶C. Fiorino, M. Reni, A. Bolognesi, G. M. Cattaneo, and R. Calandrino, "Intra- and inter-observer variability in contouring prostate and seminal vesicles: Implications for conformal treatment planning," *Radiother. Oncol.* **47**, 285–292 (1998).
- ⁵⁷P. Giraud, S. Elles, S. Helfre, Y. De Rycke, V. Servois, M. F. Carette, C. Alzieu, P. Y. Bondiau, B. Dubray, E. Touboul, M. Housset, J. C. Rosenwald, and J. M. Cosset, "Conformal radiotherapy for lung cancer: Different delineation of the gross tumor volume (GTV) by radiologists and radiation oncologists," *Radiother. Oncol.* **62**, 27–36 (2002).
- ⁵⁸I. El Naqa and Y. Yang, in *Medical Imaging Systems: Technology and Applications*, edited by T. Leondes (World Scientific, Singapore, 2005), Vol. 4, pp. 15–36.
- ⁵⁹X. F. Zha, *Artificial Intelligence and Integrated Intelligent Information Systems: Emerging Technologies and Applications* (Idea Group, Hershey, 2007).
- ⁶⁰P. Viola, *Alignment by Maximization of Mutual Information* (MIT, Cambridge, MA, 1995).
- ⁶¹K. K. Brock, L. A. Dawson, M. B. Sharpe, D. J. Moseley, and D. A. Jaffray, "Feasibility of a novel deformable image registration technique to facilitate classification, targeting, and monitoring of tumor and normal tissue," *Int. J. Radiat. Oncol. Biol. Phys.* **64**, 1245–1254 (2006).
- ⁶²I. El Naqa, D. A. Low, S. Wahab, P. Parikh, M. Nystrom, J. Hubenschmidt, J. O. Deasy, I. A. Amin, G. Christensen, and J. Bradley, "Automated 4-D lung computed tomography reconstruction during free breathing for conformal radiation therapy," in *Medical Imaging, San Diego, CA, 2004* (SPIE, San Diego, 2004).
- ⁶³P. Keall, "4-dimensional computed tomography imaging and treatment planning," *Semin. Radiat. Oncol.* **14**, 81–90 (2004).